Inductive Power Transfer System With Self-Calibrated Primary Resonant Frequency

Aref Trigui, Sami Hached, Faycal Mounaim, *Member, IEEE*, Ahmed Chiheb Ammari, *Member, IEEE*, and Mohamad Sawan, *Fellow, IEEE*

***Abstract*—Inductive power transfer (IPT) is a commonly employed technique for wirelessly supplying power to implantable medical devices. A major limit of this approach is the sensitivity of the inductive link to coupling factor variations between transmitting and receiving coils. We propose in this paper a new method for compensating these variations and improving the inductive link efficiency. The proposed technique is based on a mechatronic module that dynamically tunes the primary resonant capacitor value in order to maintain the resonance state of the IPT system. The module is able to maintain resonance state for apparent primary inductance range at least from 0.5 to 5 μH using a high capacitance resolution of 0.032 pF. Experimentations conducted on a 13.56-MHz IPT system showed a 65% higher power transfer compared to a traditional IPT system.**

***Index Terms*—Class E amplifier, feedback circuits, implantable biomedical devices, inductive power transmission.**

I. INTRODUCTION

DURING the last decades, implantable medical devices (IMDs) changed the landscape of modern medicine. Combining many technologies and employing smart medical devices within the human body, they allowed a continuous and automatic management of numerous health issues, such as urinary function rehabilitation [1], [2]. Due to their continuously increasing potential, IMDs are getting more complex thus requiring more energy to operate. These devices are usually powered through embedded batteries [3]. Since the amount of energy in batteries is limited, a wireless charging technique is used in order to avoid surgery for battery replacement. Several efforts have been made to develop reliable wireless powering transfer systems for IMDs. Many wireless power transfer (WPT) methods were proposed in the literature including: RF link [4], optical link [5], [6], ultrasonic [7], [8], capacitive link [9], thermo-electric power generators [10], permanent magnet coupling [11], and inductive link [12]. Due to its simplicity, reliability and safety, the inductive link is the most adopted technique in commercial IMDs [13]. Although inductive links were originally designed for wireless powering, they offer the capability of bidirectional data transmission.

The principle of a traditional inductive power transfer (IPT) system (see Fig. 1) is based on two coils positioned in proximity to each other. When an ac current flows through the primary coil, an ac magnetic flux is created in its vicinity. This flux is picked-up by the secondary coil and therefore converted to an ac voltage across it. The IPT system is composed of an external power transmitter and a power receiver implanted inside the human body. The power transmitter is mainly composed of an oscillator and a power amplifier (PA) that generates an ac current at a specific frequency and amplitude. A tuning capacitor is placed upstream of the primary coil with another tuning capacitor in the receiver located downstream of the secondary coil. Each of them forms an *LC* circuit in order to ensure resonance state and maximize the power efficiency. In the receiver, a rectifier and a dc–dc converter convert ac power to a regulated dc intended to supply the load with the needed current. Although the IPT has been widely deployed in various medical devices for a long time, it still has some limitations. The inductive link sensitivity to load and coupling variations is among the major drawbacks. Yet, the coupling variation impact on efficiency remains significant and among the most popular research topics in IMDs.

Two classical implementation approaches were employed in order to reduce the IPT system sensitivity to misalignment and indirectly to coupling variation [14]. The first method is called the geometric approach, which consists of using a primary coil (L_1) larger than the secondary one (L_2). That way, L_2 remains inside the perimeter of L_1 for some degree of coil displacement. The second technique is called the stagger-tuning approach, where the resonance frequencies of both circuits (energy emitter external circuit, and receiver implantable one) are intentionally separated from each other and the operating frequency is selected among them. With these two energy transfer methods, the sensitivity to coupling variation is reduced at the expense of power transfer efficiency. Both approaches also require a high-coupling factor of inductive link which is not always the case for biomedical applications of IPTs due to the presence of harsh environment (absorption through the numerous body layers such as skin, fat, etc.) and receiver noncontrolled displacement [15].

More advanced control loops have been proposed to improve efficiency. Actually, a good efficiency is ensured when the primary and secondary circuits resonate at the same operating frequency. Nevertheless, the resonance frequencies vary according to the link parameters in both side of the link. Consequently, feedback or closed-loop circuits are usually employed on both sides in order to compensate these variations. These control circuits and algorithms are usually complex and require a long tuning delay to achieve a reliable calibration [16]. Furthermore,

Manuscript received September 30, 2014; revised December 9, 2014; accepted January 19, 2015. Date of publication February 2, 2015; date of current version July 10, 2015. This work was supported by the Canada Research Chair on Smart Medical Devices and by the University Mission of Tunisia in North America. Recommended for publication by Associate Editor A. Covic.

A. Trigui, S. Hached, F. Mounaim, and M. Sawan are with Electrical Engineering Department, Polytechnique Montreal, Montreal, QC H3T 1J4 Canada (e-mail: aref.trigui@polymtl.ca; sami.hached@polymtl.ca; faycal.mounaim@polymtl.ca; mohamad.sawan@polymtl.ca).

A. C. Ammari is with the Electrical and Computer Engineering Department, King Abdulaziz University, Jeddah 22254, Saudi Arabia, and also with MMA-INSAT, Carthage University, Carthage 1054, Tunisia (e-mail: ac.ammari@yahoo.fr).

Color versions of one or more of the figures in this paper are available online at http://ieeexplore.ieee.org.

Digital Object Identifier 10.1109/TPEL.2015.2399417

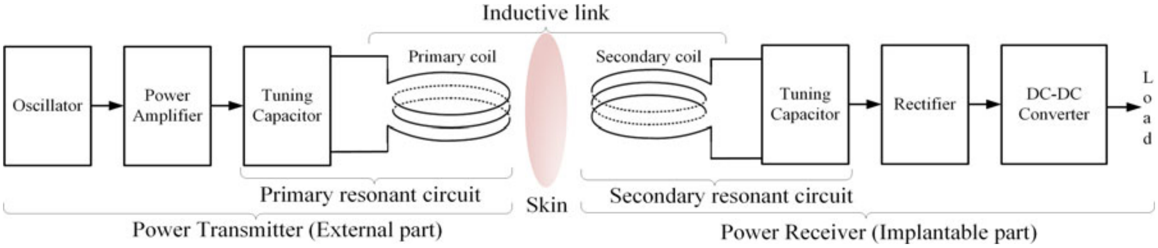

Fig. 1. Typical model of an IPT system for IMDs.

calibration at both sides is not suitable for systems requiring a small size and a low-power consumption at the receiving side as is the case of IMDs. Knowing that the resonant primary circuit is more sensitive to coupling variation [15], it is more practical and less complex to improve the link efficiency by acting only on the primary side. To maintain resonance state at primary side, there are three main control methods as described below.

A. Operating Frequency

This method consists of tracking and controlling the primary resonant frequency variation [17] [18]. In this case, the operating frequency may exceed the allocated bandwidth for wireless network regulation. For example, in the used Industrial, Scientific and Medical (ISM) radio bands of $13.56\ \mathrm{MHz}$, the range is $13.56\ \mathrm{MHz} \pm 7\ \mathrm{kHz}$ [19] which is a narrow bandwidth for calibration. In addition to these restrictions, the receiver must resonate at a frequency closer to the operating frequency to achieve an appropriate power transfer efficiency. This requires additional control loop in the secondary side rendering the design complex.

B. Primary Inductance

The second method relies on employing a transductor whose inductance value is electrically controlled [20], [21]. This method provides a stable operating frequency but leads to a bulky system hardware that is inappropriate for portable devices.

C. Primary Capacitance

This third method consists of controlling the capacitance of the primary circuit. This capacitance can not be easily tuned using a varicap diode due to the presence of high-voltage and high-current variations in the primary resonant circuit [22]. The dynamic variation of the resonant capacitor can also be achieved with a bank of switchable capacitors whose value is tuned upon requests received from the secondary side. In [23], the optimum primary capacitance is determined after a number of increments/decrements of the capacitor-bank value with a resolution of $100\mathrm{pF}$, such that the received and rectified output voltage in the secondary side is maximized. Note that with this method, the resolution and the capacitance range can be improved by adding more capacitors and switching devices, but then it would be at the expense of the system size and complexity.

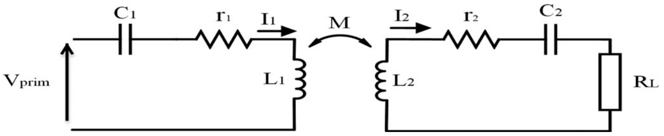

Fig. 2. Circuit model of a series-series inductive link topology.

In this paper, we propose a novel concept for compensating inductive link coupling variations. In proposed method, the primary resonant frequency calibration is achieved thanks to a mechatronic module that mainly consists of extending the variation of the capacitor values between 25 and 500 pF driven by a miniature and high-resolution stepper motor, along with voltage detector located in the primary coil allowing real-time measurement of the transmitted power to the implanted device [24]. The remaining parts of this paper include in Section II the basic concepts and analyses commonly employed in IPT systems, as well as the theory and simulations applied to demonstrate the proposed calibration technique. The description of the circuit and system parts are the subject of Section III, altogether with the design considerations and challenges. Experimental results and measurement procedures will be presented and discussed in Section IV.

II. IPT FUNDAMENTALS

Based on capacitors and coils arrangement, four main inductive link topologies are used to build the required serial or parallel resonant circuits, which combine one type of secondary circuit along with one type of primary circuit. In this study, the series-series topology, presented in Fig. 2, is adopted for reasons of simplicity and common understanding of the coupling variation impact on the inductive link performance.

The level of interaction between two mutually coupled coils may be presented using two parameters: the mutual inductance *M* and the coupling factor *k*. These parameters depend strongly of the coils geometry (size and shape), relative position (distance and angle) and material properties. Expressing precisely these factors is not an easy task. However, Roz and Fuentes have estimated them by [25]

$$k = M/\sqrt{L_1 L_2} = \frac{r_{L1}^2 r_{L2}^2 \cos\theta}{\sqrt{r_{L1} r_{L2}}\left(\sqrt{D_a^2 + r_{L1}^2}\right)^3} \tag{1}$$

where r_{L1} and r_{L2} are the radii of the primary and secondary coils; D_a and θ are the axial distance and the angle between the

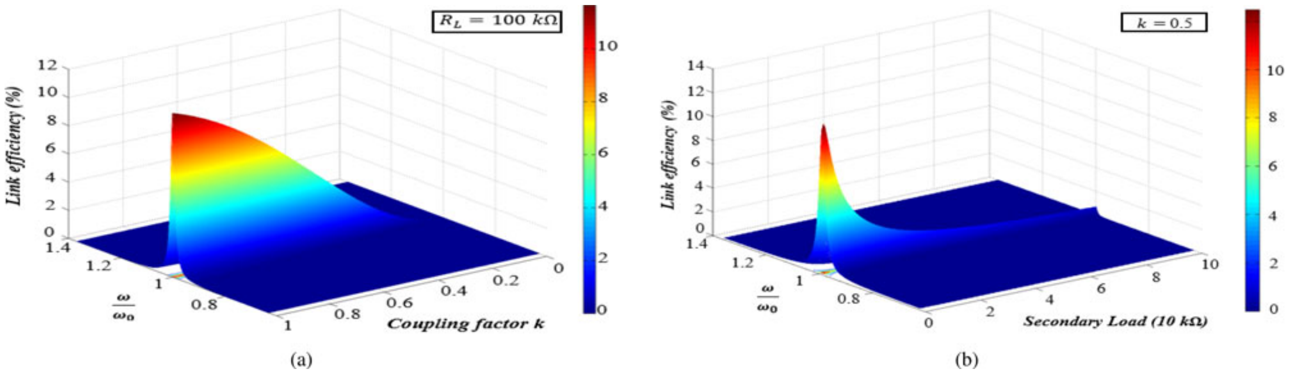

(a) (b)

Fig. 3. Link efficiency η_{link} versus the normalized angular frequency for different values of (a) coupling factor k (for $R_L = 100\ \text{k}\Omega$), and of (b) secondary load R_L (for $k = 0.5$).

coils, respectively. Note that (1) is only applied when the radii of the coils satisfy the condition $r_{L2} \leq r_{L1}$.

Another important parameter in IPT systems is the quality factor Q of the coils. The higher it is, the better the link efficiency is [26]. The quality factor Q represents the ratio between the reactance and the real part of its impedance

$$Q_1 = \omega L_1 / r_1 ; Q_2 = \omega L_2 / r_2 \tag{2}$$

where r_1 and r_2 are, respectively, the internal series resistances of primary and secondary coils.

Prior to discussing the impact of the coupling variation on the inductive link efficiency, the resonance-state's impact on the link efficiency must be assessed. The link efficiency η_{link} can be calculated in several ways [27]–[29]. However, the approximate expression of η_{link} given by [30] can reveal the resonance-states impact on the link efficiency by assuming that the resonant frequencies are equal to each other $(\omega_{r1} = \omega_{r2} = \omega_0)$. A numerical verification under MATLAB of that expression, for $f_0 = 13.56\ \text{MHz}, L_1 = L_2 = 0.8\ \mu\text{H}, r_1 = r_2 = 0.7\ \ \Omega$, clearly shows that regardless of k and R_L, the link efficiency reaches its maximum value when the operating frequency equals the resonant frequency, and decreases while moving away from ω_0 (see Fig. 3). This ensures that the resonance condition $(\omega = \omega_0)$ is fundamental to improve the link efficiency [31].

As mentioned previously, the resonant frequencies vary in response to coupling variation. This phenomenon, known as splitting frequency, is widely reported in magnetic resonance WPT system, recently proposed by an MIT research group [32], [33]. It occurs when the coupling factor k between the transmitter and the receiver is higher than the splitting coupling k_{split}. In this state, two new resonant frequencies appear (which allow a maximum of power load P_{R_L}) instead of a single one. These frequencies located on either side of the operating frequency are designated by the odd and the even splitting frequencies. They are determined by using the splitting equation

$$\partial P_{R_L} / \partial \omega = 0 \tag{3}$$

where the load power P_{R_L} is expressed in (4) [33]

$$P_{R_L} = \frac{\omega^2 M^2 R_L V_{\text{prim}}^2}{(\omega^2 M^2 + r_1 R_2 - X_1 X_2)^2 + (R_2 X_1 + r_1 X_2)^2} \tag{4}$$

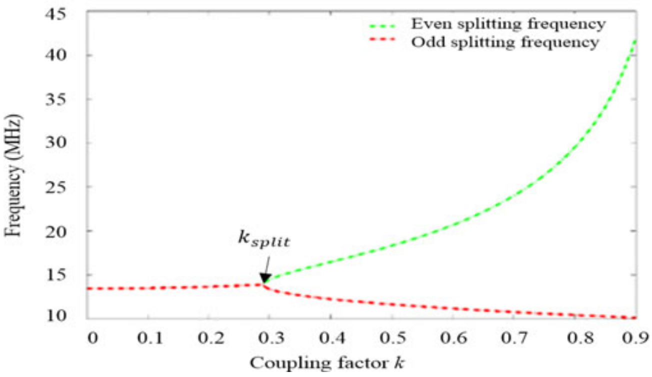

Fig. 4. Splitting frequency phenomenon.

with $R_2 = r_2 + R_L$, $X_1 = L_1\omega - \frac{1}{C_1\omega}$, and $X_2 = L_2\omega - \frac{1}{C_2\omega}$.

To solve (3), a symmetrical system is adopted. Thus, the electrical parameters of the primary and secondary sides are equal $(L_1 = L_2 = L, C_1 = C_2 = C, \text{and}\ R_L = R)$. According to the study reported in [33], the splitting coupling, the odd and the even splitting frequency take the following expressions:

$$k_{\text{split}} = (1/Q)\sqrt{1 - 1/4Q^2} \tag{5}$$

$$f_{\substack{\text{even}\\ \text{odd}}} = f_0 \sqrt{\frac{(2 - Q^{-2}) \pm \sqrt{(2 - Q^{-2})^2 - 4(1 - k^2)}}{2(1 - k^2)}} \tag{6}$$

with $Q = \omega_0 L / R$.

We can notice that when $k = k_{\text{split}}$, both frequencies converge to the splitting frequency f_{split}

$$f_{\text{split}} = f_0 / \sqrt{1 - 1/(2Q^2)}. \tag{7}$$

It is also noticeable that by increasing the Q factor, the splitting frequency f_{split} will tend to reach the natural resonant frequency f_0. This frequency splitting phenomenon is illustrated in Fig. 4, using (6) with $f_0 = 13.56\ \text{MHz}, L = 2\ \mu\text{H}, \text{and} R = 50\ \Omega$. For a coupling factor higher than $k_{\text{split}} (= 0.29)$, two resonant frequencies appear and diverge from each other as the coupling factor increases. In addition, when the coupling factor

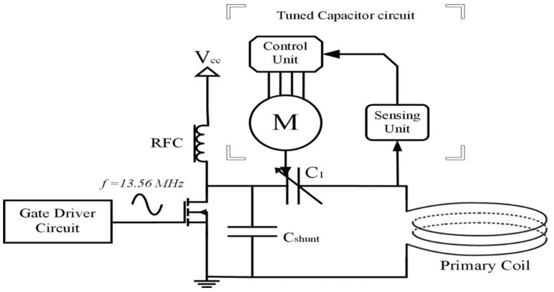

Fig. 5. Simplified block diagram of the proposed inductive power transmitter.

k is at its maximum value ($k \to 1$), the even splitting frequency tends to infinity and the odd splitting frequency is defined as $f_{\rm odd} = f_0/\sqrt{2}$. This indicates that the increase of the $f_{\rm even}$ is much faster than the decrease of the $f_{\rm odd}$. Therefore, if a splitting frequency tracking system is used, the odd splitting frequency $f_{\rm odd}$ must be selected since it has a relatively smaller variation. On the other hand, if the operating frequency f should be constant, the resonant frequencies can be brought back to the natural resonant frequency f_0 by varying the capacitance or inductance of the two resonant circuits as previously discussed. We can observe in Fig. 4 that the splitting frequency is significant when the coupling factor value is increased. In fact, for $k = 0.9$, the odd splitting frequency $f_{\rm odd}$ reaches a frequency of 10 MHz which is equivalent to a difference of 3.56 MHz compared to the natural resonant frequency. Therefore, returning back to the resonant-state, requires a capacitance variation of

$$\Delta C = 1/(4\pi^2 L_{\rm eff1}(f_0 - f_{\rm odd})^2) = 543\, pF \tag{8}$$

where $L_{\rm eff1}$ being the total primary effective inductance when $f_{r1} = f_{\rm odd}$ and C_1 at its original value $(\frac{1}{4\pi^2 L_1 f^2} = 68.8\ \text{pF})$

$$L_{\rm eff1} = 1/(4\pi^2 C_1 f_{\rm odd}^2). \tag{9}$$

This confirms that the compensation capacitor must reach large values to cover a wide range of coupling variation. In order to prevent the hard switching problem that occurs in capacitor arrays controlled by power transistors, and in order to guarantee a wide range of capacitance variation with high resolution, we proposed the use of a tunable capacitor and a calibration mechanism based on a high-resolution miniature stepper motor. This implemented and validated method allowed smooth capacitance value variation without parasitic ripple.

III. MATERIALS AND METHODS

Fig. 5 illustrates a simplified schematic of the proposed wireless power transmitter. It can be split into two main parts; the first one is the traditional inductive power transmission circuit. It integrates a gate driver circuit that generates a sinusoidal waveform at 13.56 MHz, applied to the transistor forming class E PA. This PA provides maximum energy when the primary resonant circuit is tuned to equal the operating frequency. The second part is the tuned capacitor circuit that is composed of a sensing circuit, a control unit and a miniature stepper motor. The sensing circuit measures the positive peak of the primary coil ac voltage. Following attenuation and conditioning, this acquired signal is fed into a control unit that controls the high-resolution stepper motor. The motor shaft is attached to a foil trimmer capacitor C_1, which is exceptionally small for its maximum capacitance of 500 pF. Given that, each motor step induces a small capacitance variation. More details on each element of the proposed system will be explained in this section.

A. Implementation of the Inductive Power Transmission System

1) Gate Driver Circuit and Operating Frequency Selection: With its oscillator and amplifier, the implemented circuit drives the PA operating at the desired frequency. Among several types of oscillators, the quartz crystal-based oscillator was selected due to its frequency accuracy. It is designed according to the Colpitts configuration whose main advantages reside in its simplicity of implementation and its robustness. However, the output current of the oscillator is not high enough to drive the considerable gate capacitance of the power MOSFET at 13.56 MHz frequency. Indeed, at this relatively high frequency, the gate driver circuit must provide a high-current level during a very short duration in order to reduce the switching loss. Consequently, we added to the oscillator a high slew-rate and sufficient output current buffer amplifier. On the other hand, the 13.56 MHz frequency is selected inside the high frequency part of the ISM band, which is allocated for medical applications. Operating in the ISM band gives us the opportunity to transmit the permitted power budget without requiring special frequency authorization from the regulatory authorities [35]. Power transmission at this frequency is safer than using the ultra-high frequency band of ISM or the Medical Implant Communication Services band. At ultra-high frequencies, a wireless link of few meters can be achieved. However, tissue heating and potential damage prevents the operation at these frequencies in IPT. This explains the reason why the frequency used in inductive links is typically below 30 MHz [36].

Fig. 6(a) shows the limit values of the magnetic field strength in this range, which are allowed in case of an enclosed, coil area $< 30\ m^2$. Surely, the authorized field strength at low-frequency is higher than at high-frequency band since the tissue heating effect at low frequencies is negligible. Nevertheless, the wireless transmission range between the coils is relatively short. From Fig. 6(b), a measurement of the wireless range of an inductively coupled link with the same magnetic field strength $(105\ dB\mu A/m)$ at different frequencies, shows that the powering range is maximized around 10 MHz. Besides, given that a higher frequency allows both smaller coil and resonant capacitor dimensions on both sides of the link, the frequency of 13.56 MHz is considered the most appropriate since it provides a good compromise between the three following parameters: the permitted magnetic field strength, the wireless transmission range and the system size.

2) Class E PA Design: The PA is the core of the wireless power transmitter. A dedicated PA is necessary to drive the primary coil in order to generate the required magnetic field. There are several types of PA that can be used in IPT systems [37]. Class D and class E PAs are the most commonly used in biomedical applications requiring inductive links due to their

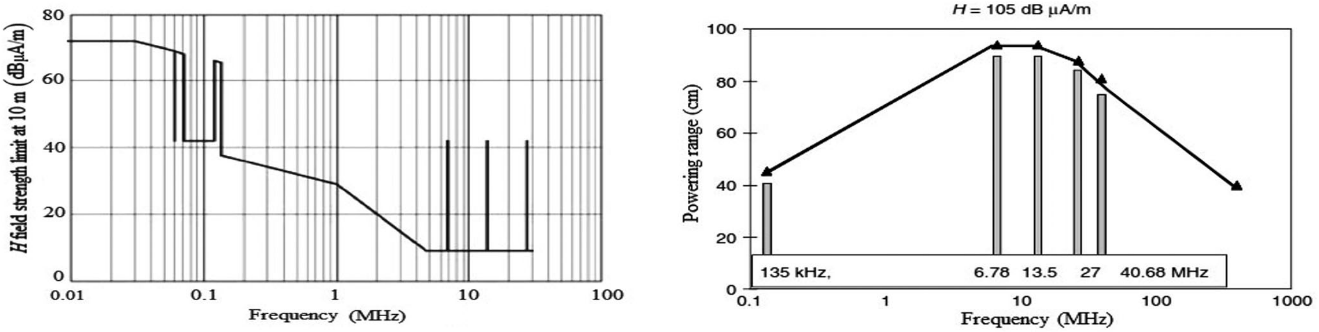

(a) (b)

Fig. 6. ISM frequency versus (a) maximum permitted magnetic field (H) strength measured at a distance of 10 m, and (b) wireless range at the same magnetic field strength [34].

100% theoretical efficiency. Nevertheless, the class E topology was chosen because, unlike the class D topology, it has only one active element instead of two. This feature reduces the gate driver power dissipation and avoid the simultaneous conduction of both transistors. The latter event creates a low-resistance path from the supply to the ground through these transistors, which induces a large shoot-through current resulting in transistors heating up and eventually being damaged.

Among the elements to be considered when designing a class E PA that minimizes power losses is the switching transistor, the MOSFET is a common choice in high frequency switching applications. Due to its greater mobility of electrons, n-type MOSFET has a low drain-source ON-state resistance R_{DSon} and is therefore better than the p-type for our application. This ensures a low conduction power loss

$$P_c = R_{\mathrm{DSon}} I_{ds}^2. \tag{10}$$

However, reduction of R_{DSon} leads normally to an increase in the gate capacitance and the gate charge Q_g. Thus, a high gate capacitance increases the gate driver power loss

$$P_g = V_{\mathrm{gate}}^2 C_{\mathrm{gate}} f \tag{11}$$

where C_{gate} is the equivalent input capacitance of the MOSFET and V_{gate} is the voltage level applied at the gate.

Parasitic intrinsic elements also induce losses during On-Off transition states, known as switching losses. These losses are difficult to avoid especially at high-operating frequencies (above 2 MHz) due to the dissipation of the charge stored in the parasitic capacitance or due to inductive energy stored in the parasitic inductances [38]. Unfortunately, the transistor intrinsic elements are highly interdependent and improving one parameter can degrade indirectly the others. Therefore, a tradeoff between intrinsic components and a suitable choice of the buffer amplifier must be made. For the proposed implementation, the SH8K5 transistor from Rohm Semiconductor was used as the nMOS transistor allowing fast switching and a maximal drain-source voltage and current of 30 V and 3 A, respectively. This transistor was selected due to its acceptable tradeoff between the drain-source ON-state resistance ($R_{\mathrm{DSon}} = 93\ m\Omega$) and the typical input capacitance ($C_{\mathrm{gate}} = 140$ pF). In addition, the buffer amplifier LM7171 from Texas Instruments was employed as a gate driver. Its very high slew rate of $4100\ V/\mu s$ and output current of $100\mathrm{mA}$ are adequate to efficiently drive the nMOS transistor at 13.56 MHz.

TABLE I
FEATURES OF THE SELECTED TRIMMER CAPACITOR

Capacitance range (pF)		Breakdown voltage (V)	Temperature stability (ppm/C)	Dimension (mm)	$Q_{\min}$ $(1\ MHz)$
Min	Max				
25	500	200	350	L= 10 W= 12 H= 14	300

As shown in Fig. 5, the power nMOS transistor drives an LC output network integrating a capacitor in parallel also called shunt capacitor C_{shunt}, a primary coil (L_1) and a series-tuned capacitor (C_1). It has been proven that only C_1 has a significant impact on the resonant-state of the class E amplifier [23], where C_{shunt} and the intrinsic output capacitor of the transistor are mainly used as an alternative current pathway when the switch is off, in order to reduce power dissipation in transistor. Other design considerations were adopted such as, the use of a sufficiently large RF coil choke (RFC=1 mH) to ensure a dc current source with minimal ripples then the reduction of the parasitic resistances, by decreasing the PCB tracks length, for a high quality factor. Indeed, the series-resonant circuit must have a high quality factor Q to achieve sufficient selectivity allowing only the fundamental component of the gate drive signal to reach the coil. So typically, to deliver the maximum energy at a fixed power supply V_{cc}, the L_1C_1 circuit should resonate at the same frequency as the switching frequency. However, a variation in coupling factor k can modify the resonant frequency causing an out-of-resonance operation and consequently a low power transfer efficiency and low induced field.

In order to operate continually in resonance and compensate this variation, a controlled polyimide trimmer capacitor has been used. Such dielectric material provides a high-breakdown voltage and a good tradeoff between the size and the capacitance range. The selected capacitor (109 9601 500 from DAU) has a compact size and provides a maximum capacitance of 500 pF. Its quality factor and its maximum breakdown voltage are also suitable for our application. The features of this capacitor are shown in Table I. The transmitter shows high flexibility for the primary coil value and high immunity against large coupling variations. Indeed, thanks to a primary capacitor that is tunable

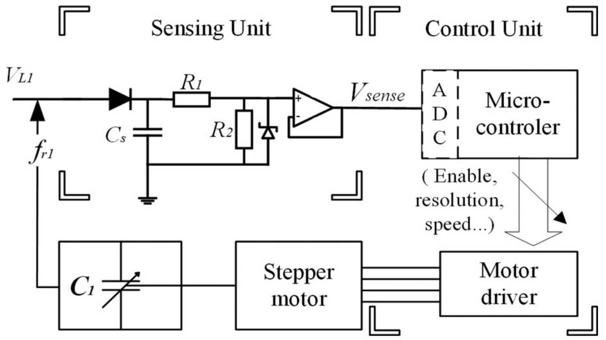

Fig. 7. Prototype of the proposed power transmission system.

from 25 to 500 pF, the transmitter is capable of adapting and maintaining resonance across a wide primary coil inductance range, roughly from 500 nH to 5 μH. The design and the control principle of the tuned capacitor circuit are discussed in this next section.

B. Tuned Capacitor Circuit Design

Fig. 7 shows the schematic of the proposed tuning capacitor circuit. It is composed of a peak voltage detector, a resistor-based divider followed by a buffer, a microcontroller integrating an ADC circuit, a micro stepping driver, and a miniature stepper motor that drives the series-trimming capacitor.

Laws of physics have already demonstrated that at resonance state in LC circuit, the peak voltage at the coil's terminal reaches its maximum value. Based on this fact, we designed a peak detector of the primary coil voltage V_{L_1} using the traditional single-diode half-wave rectifier circuit. The rectified voltage is then attenuated by a resistor-based voltage divider and applied to the ADC built-inside the microcontroller via a zener diode protection and unity gain buffer. The resistance values of the attenuator were chosen to constantly provide an output voltage (V_{sense}) less than the maximum permitted ADC input voltage, which is equal to 5 V. Aiming at a maximum primary coil peak voltage up to 75 V, R_1 and R_2 values are set to $4.7\text{M}\Omega$ and $340\text{k}\Omega$, respectively. On the other hand, the value of the smoothing capacitor C_s is carefully chosen in order to achieve accurate detection. Indeed, it is necessary to have a capacitor through $R_{eq}(= R_1//R_2)$ between two positive half cycles of V_{L_1}. Also, V_{sense} must follow the variation of V_{L_1} defined by the motor stepping frequency f_{MS} that reaches few kHz. Hence, according to (12), a value of 0.1nF of C_s should be able to properly track the variation in the primary coil positive peak

$$1/(13.56\ MHz) \ll \tau(R_{eq}C_s) \ll 1/f_{MS}. \tag{12}$$

After sampling V_{sense} by its internal ADC, the microcontroller controls the stepper motor through a microstepping driver according to predefined parameters (speed, direction and resolution). It can also inform the user about the system status and the peak voltage value at the coil's terminal via an alphanumeric LCD screen.

The microstepping driver provides the required power to run the stepper motor and allows splitting each full step into smaller steps (or microsteps). The adopted DRV8834 from Texas instruments offers six step-modes or resolutions (full, half, $1/4, 1/8, 1/16$, and $1/32$ steps). For the stepper motor, the selection criteria were mainly the size and the resolution. The motor used (PG20L-D20-HHC0 NMB Technologies Corporation) has a small dimension of $\oslash 20\ mm\ \times 45\ mm$ and a resolution of 1818 steps per revolution, which corresponds to an angle of $0.198°$ per step. However, this is just a theoretical value, because small position error may occur due to the difference in mechanical precision of the stator and rotor. The used stepper motor has a step accuracy of $\pm 5\%$ $(\pm 0.01°)$ and this error is non-cumulative from one step to the next. The error can be neglected in full-step mode. Nevertheless, increasing resolution decreases the microsteps accuracy. For example, if the mode $1/32$ was adopted, the angle in each step is $0.006° \pm 0.01°$ (accuracy is the same because it depends on the motor mechanical precision). With a positioning error higher than 100%, this resolution cannot be used. A good resolution-accuracy tradeoff can be achieved using eighth-step mode. With this configuration, the motor rotates with an angle of $0.024°$ per step with an error of $\pm 0.01°$. To vary the primary adjustable capacitor, the motor shaft is attached to the adjustable capacitor by means of a small trimmer tool. That way, the stepper motor is able to vary the capacitance value and eventually the primary resonant frequency at each covered step. In fact, the resulting driver-motor/adjustable capacitor provides a theoretical capacitance variation of 0.032 pF for each motor step. Another important aspect tackled in this study is the motor assembly. Initially, the motor has been mounted vertically. Although this configuration ensures proper operation, it considerably increases the package volume. To overcome this problem, we designed an ABS plastic holder that allows us to mount the motor horizontally as shown in Fig. 8. Moreover, the motor occupies only 11% of the overall $9.5 \times 11.0\ cm^2$ PCB prototype area. Hence, the prototype can be easily carried or attached to a belt. As soon as the circuit is activated by the user through a push button, the stepper motor covers a complete revolution. For each step, the microcontroller compares the current V_{sense} value with the maximum voltage ($V_{\text{sense}_{\text{max}}}$) detected in previous crossed steps. By the end of the revolution, the microcontroller determines the position of the most suitable compensation capacitance value. Consequently, the microcontroller drives the motor to reach the digitally saved angular position.

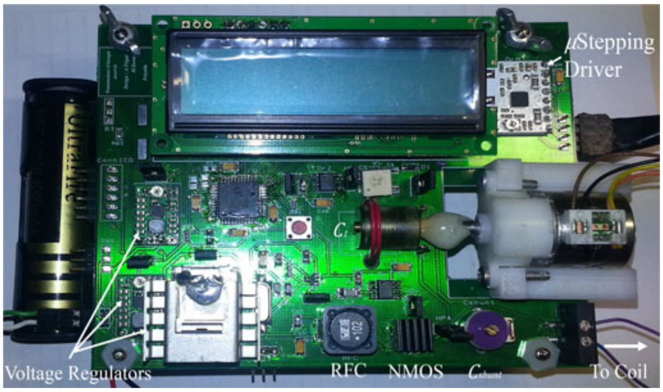

Fig. 8. Prototype of the proposed power transmission system.

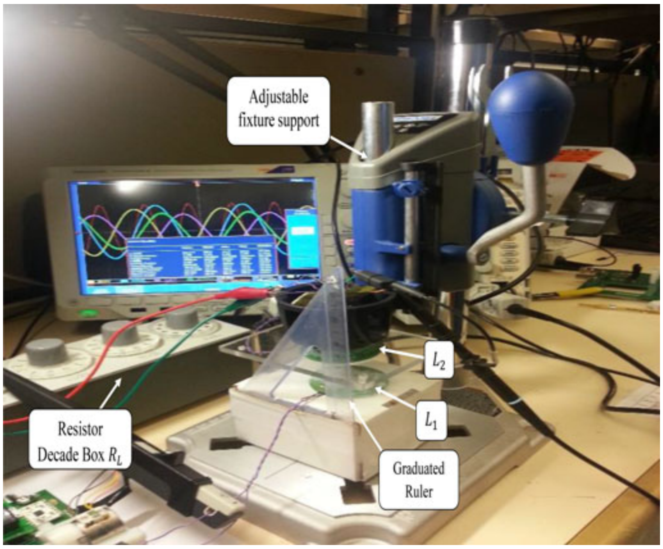

Fig. 9. Photograph of the experimental setup.

After the first execution, when coils misalignment occurs and the voltage difference between V_{sense} and $V_{\text{sense}_{\max}}$ exceeds a preconfigured threshold, the same tuning cycle is reexecuted. That way, the wireless transmission is continuously monitored and the compensation is automatically performed when needed. The whole system uses two $4000\ mAh$ rechargeable lithium batteries assembled in series with an overall output voltage of $7.4\ V$. These batteries power three-voltage regulators in order to supply the various circuit parts: two inductor-based switching regulators with output voltages of $5\ V$ (for the oscillator, microcontroller, microstepping driver and buffer amplifiers) and $10\ V$ (for the stepper motor), and a linear regulator with adjustable output voltage V_{cc} (1 to $2.5\ V$) for the class E PA.

IV. MEASUREMENT RESULTS

The transmitter prototype was built (see Fig. 8) and tested. Fig. 9 shows the used test bench, which was specially designed in order to determine and fix the axial distance between the two coils. A common power-recovery stage was also built. It consists of a parallel resonant circuit $L_2 - C_2$, followed by a half-wave rectifier and a resistor decade box 1Ω to $1\ M\Omega$ range, which serves as secondary load R_L. For all measurements discussed in this section, the supply voltage V_{cc} was settled to 2 V and two identical coils were used on both sides. Their inductances L (840 nH) and equivalent series resistances $(ESR = 266\ m\Omega)$ were measured by an impedance analyzer.

A. Frequency and Sensing Accuracy

Fig. 10 shows an oscilloscope capture of the coil voltage and current waveforms as well as a table for harmonics measurement provided by MDO4104-6 oscilloscope. The table, inside Fig. 10, presents the amplitudes (in percent) of the first ten harmonics of the current relative to the fundamental and the total harmonic distortion in reference to the fundamental $(THD - F)$. This latter is commonly defined as the ratio of the amplitude of the harmonic components to the fundamental. Fig. 10 illustrates signals which are purely sinusoidal forms and the distortion level is very low (they do not exceed 0.5%). This ensures, at resonance, a power transfer at a very precise frequency of 13.56 MHz and also limits the power losses due to unwanted harmonics. V_{sense} is also an important parameter since it is the main link between the analog part and the digital control unit. The precision of the automatic tuning strongly depends on the accuracy of this signal, which should present a high signal to noise and interference ratio. To improve measurement accuracy, it is imperative to keep the surface loop between the probe tip and the ground alligator clip as small as possible. The signal $V_{\text{sense}_{(b)}}$, seen in Fig. 11(a), shows that a large surface loop [like in Fig. 11(b)] acts as an antenna, picking up radiated noise and adds interference to the measurement. Consequently, the best way is to use a ground tip that is wrapped right around the probe tip voltage as shown on Fig. 11(c). Since the ground tip is placed close to probe tip, the noise is decreased. By using this particular measurement method, the residual ripple was reduced by more than 95% and it is in the order of $40\ mV$ peak-to-peak.

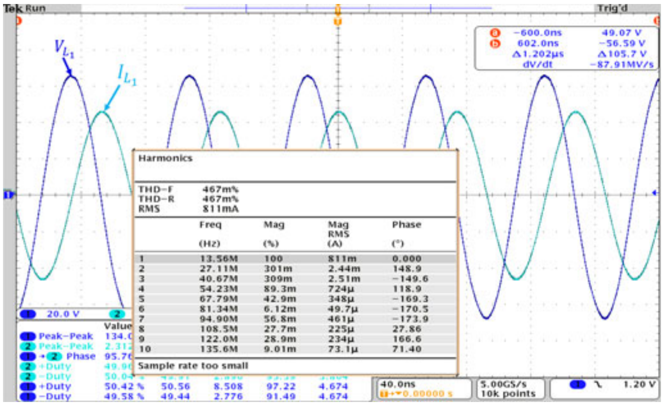

Harmonics

THD−F 467m%
THD−R 467m%
RMS 811mA

	Freq (Hz)	Mag (%)	Mag RMS (A)	Phase (°)
1	13.56M	100	811m	0.000
2	27.11M	301m	2.44m	148.9
3	40.67M	309m	2.51m	−149.6
4	54.23M	89.3m	724μ	118.9
5	67.79M	42.9m	348μ	−169.3
6	81.34M	6.12m	49.7μ	−170.5
7	94.90M	56.8m	461μ	−173.9
8	108.5M	27.7m	225μ	27.86
9	122.0M	28.9m	234μ	166.6
10	135.6M	9.01m	73.1μ	71.40

Sample rate too small

Fig. 10. Output waveforms and harmonics table.

B. Capacitor Tuning Impact on Inductive Link Performance

The evaluation of the link efficiency requires an ac power measurement at the primary and secondary coils terminals. Obviously, an ac power measurement is a point-by-point multiplication of voltage and current signals. However, each measurement probe introduces a different delay also called "Skew." The difference between these two delays depends mainly on the length of the measuring cable and the probe circuitry. To cancel the skew between voltage and current probes, a power measurement deskew fixture (067-1686-00, Tektronix) was used. The deskewing procedure is very important and must be done carefully. Even a small skew difference can cause a significant error in the measured power value, especially for high-frequency measurements. Unfortunately, despite our numerous efforts, it was impossible to obtain a repeatable measurement result and this deskewing method revealed unsuitable for accurate measurement of the link efficiency. Therefore, to accurately evaluate our proposed system, we focused on the dc load power P_{R_L} (for a fixed load $R_L = 10\ k\Omega$) and we analyzed the effect of the axial distance D_a variation on it for each of the following conditions:

1) traditional IPT system: Tuning is done once on both primary and secondary capacitors for $D_a = 1.5\ cm$, referred as "starting condition;"

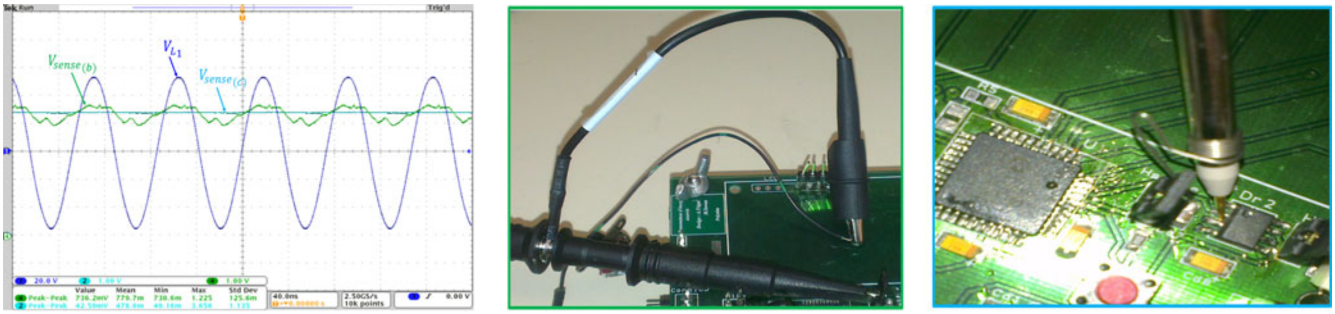

(a) (b) (c)

Fig. 11. (a) Residual ripple associated to V_{sense} signal measured with (b) nonrecommended measurement way, and (c) recommended way.

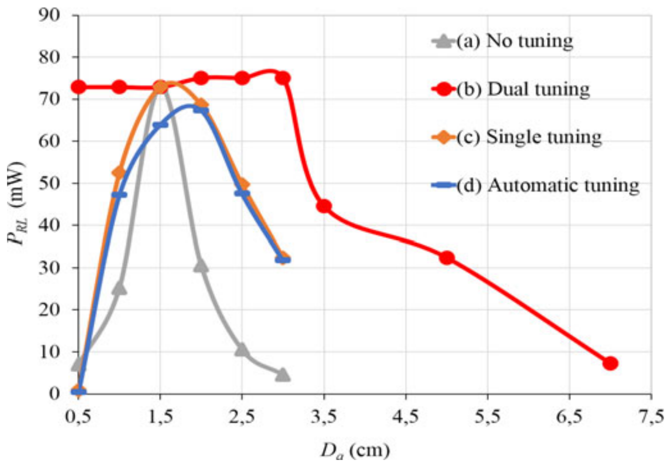

Fig. 12. Axial distance variation impact on the load power P_{R_L}.

2) manual tuning on both sides: the two capacitors C_1 and C_2 are tuned for each distance variation;
3) manual tuning of C_1: C_2 tuned only at the starting condition and C_1 tuned manually for each distance variation;
4) the proposed transmitter: C_2 tuned only at the starting condition and C_1 tuned automatically for each distance variation at rotational speed of $v_r = 0.14$ rev/s.

For conditions 1) and 2), the tuning of the two capacitors was made by observing the voltage at the terminals of the load V_{R_L}. Both resonant circuits are tuned to resonance state when the voltage V_{R_L} reaches its maximum value. Whereas, for the two other conditions, the calibration of C_1 was performed by monitoring V_{sense}, in order to evaluate the accuracy of our proposed system. The measurement results are shown in Fig. 12. Notice that the operation at resonance in both sides 2) provides a higher wireless transmission range and higher recovered power P_{R_L}. In fact, it guarantees an average improvement rate of power $(AIRP)$ of 76% compared to a traditional IPT system 1) and of 31.5% compared to 3), where $AIRP$ is defined as the average of powers differences $\Delta_{P_{R_L}} = P_{R_{L_x}} - P_{R_{L_y}}$ between two types of IPT systems x and y. Noting that $\Delta_{P_{R_L}}$ is determined at several axial distances excluding $D_a = 0.5\ cm$ and the starting condition.

However, it is important to note that the calibration of the two capacitors is a tedious task especially for small separation distances (strong coupling). A fine manual tuning was unavoidable to achieve a maximal voltage of V_{R_L}.

In addition, the calibration on both sides was performed over several steps and required a lot of time (5 min minimum). Therefore, if the dual calibration 2) is automated, the control algorithm will be complex and the system response slower.

Manual tuning of C_1 3), does not provide maximum transferred power, but it achieves a better power transfer compared to a traditional IPT system 1) ($AIRP$ of 68%), except for an axial distance of $0.5\ cm$ where a sudden drop in power occurs [seen also in trace 4)]. At this distance, $V_{\text{sense}_{\max}}$ was detected at a primary resonant frequency of 27.12 MHz (second harmonic of the gate driver signal). Based on the study of the splitting frequency discussed in Section II, this decrease in power transfer is due to excessive deviations of the resonance frequencies. The use of capacitance values beyond the preset range of C_1 did not improve the performance since the strong coupling has also detuned the secondary resonant circuit. On the other hand, the calibration of the two resonant capacitors achieved a good performance as shown in part (b) of Fig. 12. Notice that this phenomenon does not occur if C_2 is calibrated once, at strong coupling (for $D_a = 0.5\ cm$ for example). However, at this condition, the load power becomes smaller (compared to the result presented in Fig. 12) in case of a weak coupling. In that case, the following solutions can be adopted:

1) acquire the secondary voltage V_{R_L} instead of V_{sense}. That way, a better power recovery can be provided, however, adding a sensing and feedback communication system in the secondary side increases certainly the power consumption of the IMD;
2) limit the operating distance range $[D_{a_{\min}}, D_{a_{\max}}]$ and calibrate C_2 only once based on this range;
3) calibrate the two resonant capacitors. However, this method has some limitations as mentioned previously.

Our system reduces considerably the sensitivity of the inductive link to coupling variation. This can be observed in Fig. 12, and can be proved by the high $AIRP$ of 66.5% obtained by comparison with the traditional IPT system. The comparison of the single manual tuning 3) with our proposed automatic tuning 4) shows an $AIRP$ of 4% (5.5% by including the starting condition). In fact, at a speed of 0.14 rev/s, the accuracy of the stepper motor tuning seems very close to the manual tuning precision. At this velocity, the control duration interval is between 7 and 14 s, which is the time required for one to two complete motor revolution. However, a misalignment occurring during the tuning procedure can restart the process therefore causing a longer control duration. By increasing the stepper motor speed, shorter tuning duration may be achieved, but this dramatically reduces the angular position accuracy of the motor's shaft. Indeed, the higher is the speed of rotation, the lower is the holding torque. As a result, the probability of missing steps is increased which affects the system precision. A tradeoff between accuracy and control duration should be considered in such application. During the sensing process, the amount of power drawn from the PA output is only in the order of 2% of the measured power across the primary coil. Compared to the switched capacitor system reported in [23], our method provides: a smoother variation of capacitance value, a 16.5% higher transmitted power compared with a traditional IPT system and a much better capacitance resolution (0.032 pF against 100 pF). We did not compare our system with other control systems reported in the literature due to the different characteristics of each system and the lack of substantial information for comparison (such as the $AIRP$, the control duration, the resolution and the power consumption).

The proposed system in this paper still has some limitations. It was shown that an erosion of the dielectric paper of the trimming capacitor C_1 may occur, then a replacement may be needed periodically. This erosion may provoke short-circuit across the capacitor and makes its rotation axis arduous thereby degrading the precision of the automatic tuning. This confirms that this type of trimmer capacitor is not designed to be continuously tuned. A variable air capacitor can be used to improve the transmitter in order to be tuned frequently. However, this robustness is obtained at the expense of the whole system size since air capacitors are more bulky compared to dielectric trimmer capacitors. Designing a robust and miniature trimmer dedicated to our system may also be a good alternative. Adding a second feedback loop that dynamically controls the emitted power via supply voltage V_{cc} control can be another approach to reduce power losses in the internal voltage regulators and consequently in the implemented IMD.

V. CONCLUSION

In this paper, we tackled the limitation of the inductive link sensitivity to coupling variation in biomedical electronic implants. In order to reduce this sensitivity, we proposed a simple to implement and efficient capacitor-based tuned circuit operating at 13.56 MHz in the ISM band. The system is based in a new technique that controls a small stepper motor to tune the primary resonant capacitor C_1, and ensures the required primary resonance to maximize coupling efficiency. This approach reached an AIRP of 66.5% compared to a traditional IPT system and a high-tuning accuracy for a maximal control duration of 14 s with a capacitance resolution of 0.032 pF. Furthermore, the adjustable capacitor allows using of a wide inductance range varying between 0.5 and 5 μH.

ACKNOWLEDGMENT

The authors would like to thank the technical staff of Electrical Engineering Department, Polytechnique Montreal, and Tektronix Company.

REFERENCES

[1] F. Mounaim and M. Sawan, "Toward a fully integrated neurostimulator with inductive power recovery front-end," *IEEE Trans. Biomed. Circuits Syst.*, vol. 6, no. 4, pp. 309–318, Aug. 2012.

[2] S. Hached, A. Trigui, I. El Khalloufi, M. Sawan, O. Loutochin, and J. Corcos, "A bluetooth-based low-energy qi-compliant battery charger for implantable medical devices," in *Proc. IEEE Int. Symp. Bioelectron. Bioinformatics*, 2014, pp. 1–4.

[3] D. C. Bock, A. C. Marschilok, K. J. Takeuchi, and E. S. Takeuchi, "Batteries used to power implantable biomedical devices," *Electrochimica Acta*, vol. 84, pp. 155–164, 2012.

[4] E. Y. Chow, Y. Chin-Lung, O. Yuehui, A. L. Chlebowski, P. P. Irazoqui, and W. J. Chappell, "Wireless powering and the study of rf propagation through ocular tissue for development of implantable sensors," *IEEE Trans. Antennas Propag.*, vol. 59, no. 6, pp. 2379–2387, Jun. 2011.

[5] K. Goto, T. Nakagawa, O. Nakamura, and S. Kawata, "An implantable power supply with an optically rechargeable lithium battery," *IEEE Trans. Biomed. Eng.*, vol. 48, no. 7, pp. 830–833, Jul. 2001.

[6] S. Ayazian and A. Hassibi, "Delivering optical power to subcutaneous implanted devices," in *Proc. IEEE Int. Conf. Eng. Med. Biol. Soc.,* 2011, pp. 2874–2877.

[7] S. Ozeri and D. Shmilovitz, "Ultrasonic transcutaneous energy transfer for powering implanted devices," *Ultrasonics*, vol. 50, no. 6, pp. 556–566, 2010.

[8] Y. Shigeta, T. Yamamoto, K. Fujimori, M. Sanagi, S. Nogi, and T. Tsukagoshi, "Development of ultrasonic wireless power transmission system for implantable electronic devices," in *Proc. Eur. Wireless Technol. Conf.*, 2009, pp. 49–52.

[9] A. M. Sodagar and P. Amiri, "Capacitive coupling for power and data telemetry to implantable biomedical microsystems," in *Proc. 4th Int. IEEE Neural Eng. Conf.,* 2009, pp. 411–414.

[10] Y. Yang, X.-J. Wei, and J. Liu, "Suitability of a thermoelectric power generator for implantable medical electronic devices," *J. Phys. D: Appl. Phys.*, vol. 40, no. 18, pp. 5790–5800, 2007.

[11] S. Suzuki, M. Ishihara, and Y. Kobayashi, "The improvement of the noninvasive power-supply system using magnetic coupling for medical implants," *IEEE Trans. Magn.*, vol. 47, no. 10, pp. 2811–2814, Oct. 2011.

[12] S.-Y. Lee, C.-H. Hsieh, and C.-M. Yang, "Wireless front-end with power management for an implantable cardiac microstimulator," *IEEE Trans. Biomed. Circuits Syst.*, vol. 6, no. 1, pp. 28–38, Feb. 2012.

[13] F. Inanlou, M. Kiani, and M. Ghovanloo, "A novel pulse-based modulation technique for wideband low power communication with neuroprosthetic devices," in *Proc. Annu. Int. Conf. Eng. Med. Biol. Soc.*, 2010, pp. 5326–5329.

[14] A. Djemouai and M. Sawan, "Prosthetic power supplies," in *Wiley Encyclopedia of Electrical and Electronics Engineering.* New York, NY, USA: Wiley: 2009.

[15] K. Schuylenbergh and R. Puers, *The Concepts of Inductive Powering*. New York, NY, USA: Springer, 2009, pp. 41–76.

[16] T. Sun, X. Xie, and Z. Wang, *Wireless Power Management*. New York, NY, USA: Springer, 2013, pp. 123–144.

[17] N. Y. Kim, K. Y. Kim, J. Choi, and C. W. Kim, "Adaptive frequency with power-level tracking system for efficient magnetic resonance wireless power transfer," *Electron. Lett.*, vol. 48, no. 8, pp. 452–454, 2012.

[18] W. Fu, B. Zhang, and D. Qiu, "Study on frequency-tracking wireless power transfer system by resonant coupling," in *Proc. Power Electron. Motion Control Conf.,* 2009, pp. 2658–2663.

[19] F. C. Commission, "Cfr 18-industrial, scientific and medical equipment," *Code Federal Regulations*, pp. 862–868, 2008.

[20] B. Lenaerts and R. Puers, "Automatic inductance compensation for class e driven flexible coils," *Sensors Actuators A: Phys.*, vol. 145146, pp. 154–160, 2008.

[21] S. Aldhaher, P. C. K. Luk, and J. F. Whidborne, "Tuning class e inverters applied in inductive links using saturable reactors," *IEEE Trans. Power Electron.*, vol. 29, no. 6, pp. 2969–2978, Jun. 2014.

[22] F. H. Raab, "Idealized operation of the class e tuned power amplifier," *IEEE Trans. Circuits Syst.*, vol. 24, no. 12, pp. 725–735, Dec. 1977.

[23] R. Carta, J. Thon, G. Gosset, G. Cogels, D. Flandre, and R. Puers, "A self-tuning inductive powering system for biomedical implants," *Procedia Eng.*, vol. 25, pp. 1585–1588, 2011.

[24] A. Trigui, S. Hached, and M. Sawan, "Automatic control of inductive energy transmitted to electronic implants," in *Proc. Int. Symp. Wireless Power Transm.,* 2013, pp. 48–49.

[25] T. Roz and V. Fuentes, "Using low power transponders and tags for RFID applications," EM Microelectronic- Marin SA, Marin, Switzerland, 1997.

[26] M. Kesler, "Highly resonant wireless power transfer: Safe, efficient, and over distance," WiTricity Corporation, pp. 1–32, 2013.

[27] W. Zhang, S.-C. Wong, C. K. Tse, and Q. Chen, "Design for efficiency optimization and voltage controllability of series series compensated inductive power transfer systems," *IEEE Trans. Power Electron.*, vol. 29, no. 1, pp. 191–200, Jan. 2014.

[28] K. Fotopoulou and B. W. Flynn, "Wireless power transfer in loosely coupled links: Coil misalignment model," *IEEE Trans. Magn.*, vol. 47, no. 2, pp. 416–430, Feb. 2011.

[29] L. Kibok, Z. Pantic, and S. M. Lukic, "Reflexive field containment in dynamic inductive power transfer systems," *IEEE Trans. Power Electron.*, vol. 29, no. 9, pp. 4592–4602, Sep. 2014.

[30] T. Komaru, M. Koizumi, K. Komurasaki, T. Shibata, and K. Kano, "Compact and tunable transmitter and receiver for magnetic resonance power transmission to mobile objects," in *Wireless Power Transfer—Principles and Engineering Explorations.*Rijeka, Croatia: In Tech, 2011, pp. 133–150.

[31] Z.-H. Wang, Y.-P. Li, Y. Sun, C.-S. Tang, and L. Xiao, "Load detection model of voltage-fed inductive power transfer system," *IEEE Trans. Power Electron.*, vol. 28, no. 11, pp. 5233–5243, Nov. 2013.

[32] H. D. Thanh and J. I. Agbinya, "Investigation and study of mode splitting in near field inductive communication systems," *Int. J. Electron. Telecom*, vol. 59, no. 2, pp. 185–194, 2013.

[33] N. Wang-Qiang, C. Jian-Xin, G. Wei, and S. Ai-Di, "Exact analysis of frequency splitting phenomena of contactless power transfer systems," *IEEE Trans. Circuits Syst. I: Reg. Papers*, vol. 60, no. 6, pp. 1670–1677, Jun. 2013.

[34] F. Klaus, "Frequency ranges and radio licensing regulations," RFID Handbook: Fundamentals and Appl. in Contactless Smart Cards, Radio Frequency Identification and near-Field Communication, pp. 161–181, 2003.

[35] R. S. Specification, "Rss-216, wireless power transfer devices (wireless chargers), issue 1," *Spectr. Manag. Telecom*, pp. 1–8, 2014.

[36] H.-J. Yoo and C. van Hoof, *Short Distance Wireless Communications*. New York, NY, USA: Springer, 2011, pp. 219–277.

[37] M. Pinuela, D. C. Yates, S. Lucyszyn, and P. D. Mitcheson, "Maximizing dc-to-load efficiency for inductive power transfer," *IEEE Trans. Power Electron.*, vol. 28, no. 5, pp. 2437–2447, May 2013.

[38] K. Schuylenbergh and R. Puers, *Primary Coil Drivers*. New York, NY, USA: Springer, 2009, pp. 103–143.

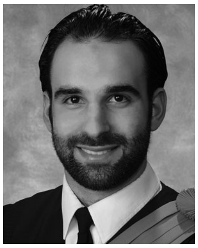

Aref Trigui graduated from the Faculty of Sciences of Bizerta, Bizerta, Tunisia, in 2010. He received the M.Sc.A. degree in electrical engineering from Polytechnique Montreal, Montreal, QC, Canada, in 2014.

He worked as Research Associate at the same institution in Polystim Laboratory. His research focus is in the area of wireless power transfer to implantable medical devices.

Mr. Trigui received the Excellence Scholarship Award from Tunisia Government to pursue his graduate studies in Canada.

Sami Hached received the Engineer degree, and the M.Sc.A. degree in automation and industrial computing from the National Institute of Applied Sciences and Technology, Tunis, Tunisia, and the Ph.D. degree in electrical engineering from Polytechnique Montreal, Montreal, QC, Canada.

He obtained 13 distinctions and prizes in artificial urinary sphincters design. His research interests include artificial sphincters, penile prosthesis and wireless power delivery to biomedical implants.

Faycal Mounaim (S'03–M'12) was born in Casablanca, Morocco. He received the M.Sc.A. and Ph.D. degrees in electrical engineering from Polytechnique Montreal, Montreal, QC, Canada, in 2006 and 2013, respectively.

His focus was on microelectronics dedicated to IMDs and his thesis proposed a highly integrated neurostimulator and a new stimulation strategy to improve micturition for paraplegics. In 2000, he joined Philips Semiconductors, Caen, France, where he received the Silver Design Award of the year 2001 for his involvement in the design of the first fully integrated silicon cable TV tuner. In 2003, he joined the Polystim Neurotech Laboratory where he became the Design and Team Leader of the Polystim Bladder Neurostimulator Project. In 2005, he worked on the technology transfer of this neurostimulator to Victhom Human Bionics. Since 2011, he is working for IPDiA, Caen, which offers an innovative semiconductor technology for higher level of miniaturization of implantable medical devices, through the integration of passives into silicon and the use of 2.5-D/3-D interposers.

Ahmed Chiheb Ammari (M'12) received the B.S. degree in electrical engineering from the National School of Engineering, Monastir, Tunisia, in 1993, and the M.Sc. and Ph.D. degrees in electrical engineering from the Institut National Polytechnique de Grenoble, Grenoble, France, in 1993 and 1996, respectively.

Since 1997, he has been Assistant, then Associate Professor in electrical engineering at Institut National des Sciences Appliques et de Technologies, Carthage University, Carthage, Tunisia. He is currently acting as an Associate Professor at the Department of Electrical and Computer Engineering, College of Engineering, King Abdulaziz University, Jeddah, Saudi Arabia. His main research interests include multicore and multiprocessor system-on-chip design, power management of battery-powered mobile systems, inductive link optimization for wireless power transfer, hybrid electrical energy storage systems and smart grid applications.

Mohamad Sawan (S'88–M'89–SM'96–F'04) received the Ph.D. degree, in 1990, in electrical engineering from Sherbrooke University, Sherbrooke, Canada.

He joined Polytechnique Montreal, Montreal, Canada, in 1991, where he is currently a Professor of microelectronics and biomedical engineering. His interests include the design and test of analog, digital, RF, and optic circuits and microsystems. He is a holder of a Canada Research Chair in smart medical devices, he is leading the Microsystems Strategic Alliance of Quebec, and is Founder of the Polystim Neurotechnologies Laboratory. He is Founder and Cofounder of several international conferences such as the IEEE NEWCAS, ICECS, and BIOCAS. He is also Cofounder and Associate Editor of the IEEE TRANSACTIONS ON BIOCAS, Deputy Editor-in Chief of the IEEE TCAS-II (2009–2013), and he is Editor and Associate Editor, and member of the board of several international journals. He is Founder and Chair of the Eastern Canadian IEEE-Solid State Circuits Society Chapter. He published more than 600 peer-reviewed papers, two books, ten book chapters, and 12 patents.

Dr. Sawan received several awards, among them the Queen Elizabeth II Golden Jubilee Medal, the Bombardier Award for technology transfer, the Jacques-Rousseau Award for achieved results in multidisciplinary research activities, the Medal of Merit from the President of Lebanon for his outstanding contributions, and the Barbara Turnbull Award for spinal cord research in Canada. He is a Fellow of the Canadian Academy of Engineering, Fellow of the Engineering Institute of Canada, and Officer of the Quebec's National Order.